Navier-Stokes Computations of Vortex Asymmetries Controlled by Small Surface Imperfections

Peter M. Hartwich*
ViGYAN, Inc., Hampton, Virginia 23666
Robert M. Hall†
NASA Langley Research Center, Hampton, Virginia 23665
and
Michael J. Hemsch‡
PRC Aerospace Technologies Division, Hampton, Virginia 23666

Navier-Stokes analyses are employed to explore the driving mechanisms controlling asymmetric vortical flows with $Re_D = 0.8 \times 10^6$ (Reynolds number based on maximum diameter) over a 3.5-caliber tangent-ogive cylinder at large angles of attack ($\alpha = 20$, 30, and 40 deg). All flowfield results are steady-state solutions to the three-dimensional, incompressible Navier-Stokes equations in the thin-layer approximation. The numerical results are in good agreement with experimental data. The major findings are 1) for $\alpha \geq 30$ deg, the vortex flows are genuinely asymmetric yet recurrent; 2) asymmetric vortex patterns are sensitive towards such parameters as machine accuracy, grid topology, etc., unless they are triggered by a slight deformation (similar to an out-of-round nose tip) in the neighborhood of the apex; and 3) for $\alpha = 20$ deg, the flow is symmetric for both circular and elliptic cross-sectional shapes of the nose tip.

Introduction

ASYMMETRIC vortex shedding arises when slender bodies, typical of missiles and fighter aircraft noses, are set at large angles of attack (typically, $\alpha \geq 30$ deg). Under these conditions, side forces occur—even for axisymmetric bodies or zero sideslip—which become so large that, while the effectiveness of control surfaces (such as vertical fins) degrades, they control the lateral stability of these vehicles. Whereas extensive data bases exist,[1-3] which can be compiled into useful guidelines for designing missiles and forebodies,[4] there are many key questions about the nature of asymmetric vortex flows over slender bodies to be answered.[5]

There is, for instance, the issue of whether asymmetries are a viscous or an inviscid phenomenon. Some experiments[4] appear to support the argument that dissimilar states of the lateral attached boundary layers cause a different separation behavior in the equatorial regime, thus leading to asymmetric vortex shedding. This is in some contrast to the computational results by Siclari and Marconi[6] for fully laminar supersonic flows over cones with asymmetric vortex pairs. These viscous results appear to support earlier inviscid analyses by Fiddes[7] and Marconi,[8] who suggested hydrodynamic instabilities as a cause for vortex asymmetries over slender bodies of revolution at large angles of attack.

Although inviscid calculations demonstrated that asymmetric vortex patterns can exist, even for symmetrically separated flows,[7,8] experiments[1-3,7] and viscous calculations[6] have shown that vortex asymmetries always feed back into the attached boundary layers leading to asymmetric separation patterns. These patterns themselves warrant some analysis, for the connection between vortex shedding and local minimum and maximum side forces has not yet been demonstrated.[5]

Another interesting phenomenon is what Hunt[5] termed the "regular" states of asymmetry. This is illustrated in Fig. 1, which uses Peter J. Lamont's surface pressure data for a 3.5-caliber tangent-ogive cylinder. (Lamont took these data while working as a National Research Council (NRC) Postdoctoral Research Associate at NASA Ames Research Center.) At a station six calibers aft of the apex, Fig. 1 shows for $Re_D = 0.8 \times 10^6$ the variation of sectional side force with roll angle for $\alpha = 20$, 30, and 40 deg. For $\alpha = 20$ deg, the flow is symmetric. For $\alpha = 30$ deg, the flow is asymmetric with the majority of the sectional side force values clustered at $|C_y| \approx 1.5$. For $\alpha = 40$ deg, just two regular states are noticed. Each of these two regular states corresponds to either maximum positive or minimum negative local side force. This

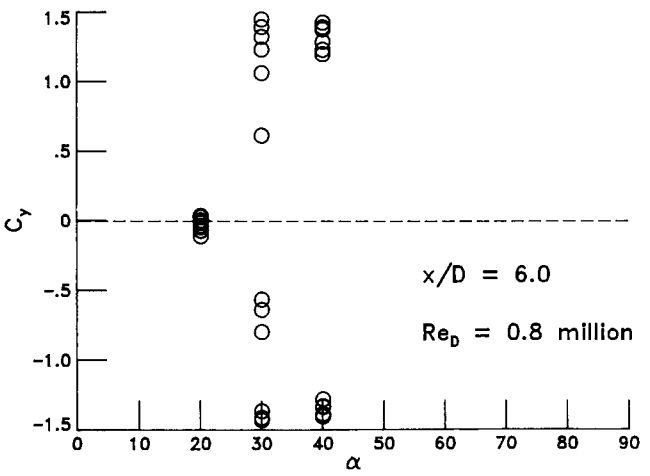

Fig. 1 Variation of sectional side force with roll angle for three angles of attack.

Received Dec. 20, 1989; presented as Paper 90-0385 at the AIAA 28th Aerospace Sciences Meeting, Reno, NV, Jan. 8-11, 1990; revision received May 16, 1990; accepted for publication May 23, 1990.

*Research Scientist. Member AIAA.
†Senior Research Engineer. Associate Fellow AIAA.
‡Engineering Specialist; currently Lockheed Engineering & Sciences Company. Associate Fellow AIAA.

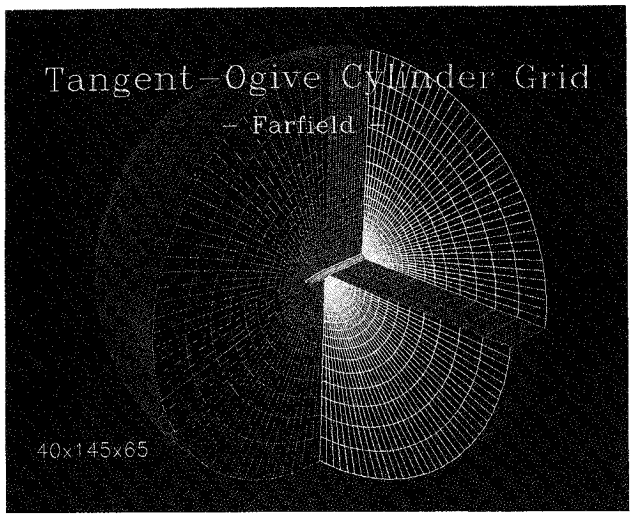

Fig. 2 Computational grid.

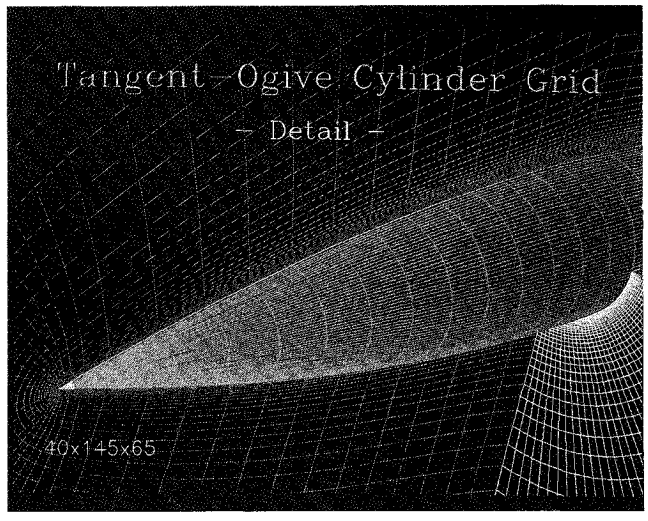

Fig. 3 Surface grid for tangent ogive.

raises the question about the causative agent that makes the asymmetric patterns lock into one of these two regular states.

Complementary to experimental efforts by Moskovitz et al.[9,10] and the analyses by Hall,[11,12] the present computational study has been initiated with the goal of demonstrating that slight perturbations of the surface geometry in the neighborhood of the apex determine the preference of the flow for one of the two regular states at high angles of attack.

As in related experiments,[1-3,9,10] the effects of compressibility are neglected, and vortical flows over a 3.5-caliber tangent-ogive cylinder are computed as steady-state solutions to the incompressible Navier-Stokes equations. Flows for $\alpha = 20$, 30 and 40 deg, and with $Re_D = 0.8 \times 10^6$, have been calculated using Fluid Mechanics Code 1 (FMC1), an implicit upwind method for computing three-dimensional, incompressible flows, which comprises flux-difference-splitting and Total-Variation-Diminishing- (TVD-) like discretizations of the inviscid fluxes.[13-16] Results are validated with experimental data, and the effects of the nose-tip shape (with either axisymmetric or slightly elliptic cross sections), of gridding, and even of the machine accuracy are discussed.

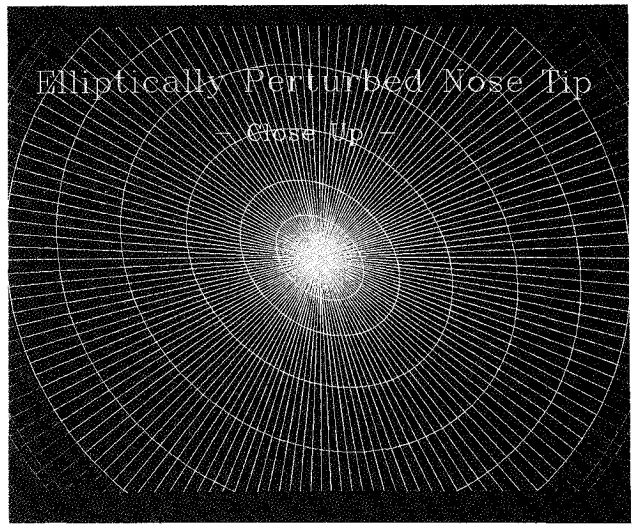

Fig. 4 Surface definition for out-of-round nose tip.

Theoretical Background

Differential Equations

The flux-vector form that is convenient for numerical simulations[17] of the three-dimensional, incompressible Navier-Stokes equations in arbitrary coordinates reads

$$(Q/J)_t + (E - E_v)_\zeta + (F - F_v)_\xi + (G - G_v)_\eta = 0 \qquad (1)$$

where t is time and J the Jacobian of the coordinate transformation. The independent variables ζ, ξ, and η describe a curvilinear, body-fitted grid. The energy equation is decoupled from the equations for mass and momentum for incompressible flows, thus the state vector Q contains only the four dependent variables p (pressure) and u,v,w (the Cartesian velocity components). The variable p is included into Q to implement Chorin's[18] artificial compressibility concept that permits construction of fast and accurate techniques to numerically solve Eq. (1).[13-16,19,20] The fluxes E, F, and G are the inviscid flux vectors. The viscous shear fluxes are given by $E_v = \hat{E}_v/(Re \cdot J)$, $F_v = \hat{F}_v/(Re \cdot J)$, and $G_v = \hat{G}_v/(Re \cdot J)$. For reasons of simplicity and efficiency,[16] Eq. (1) is solved in the thin-layer approximation

$$E_v = F_v = 0 \qquad (2)$$

without any discernible loss in accuracy for high-Reynolds-number applications.[15] The simplification due to Eq. (2) means that viscous terms are only accounted for in the direction normal to the body surface.

Equation (1) is written in nondimensional form with a reference length l_{ref} and a reference speed V_∞. The effective Reynolds number in Eq. (1) is defined as

$$Re^{-1} = Re_{lam}^{-1} + Re_{turb}^{-1} \qquad (3)$$

The eddy viscosity comprised in Re_{turb} is evaluated using a rational extension[16] to the algebraic Baldwin-Lomax turbulence model.[21] This extension allows computational modeling of transitional crossflow separation (i.e., flows with three-dimensional, equatorial separation bubbles and subsequent transition in the separating shear layers that roll up into two primary vortices). In addition, it proves to be relatively insensitive towards the choice of adjustable parameters in simulations of fully turbulent crossflow separations.

Computational Model

The implicit upwind scheme utilized in this investigation is the FMC1 method whose evolution and applications have been published many times in the open literature (see Refs. 13-16 and references cited therein). To obtain steady-state solutions independent of the time-step size, the difference

equations are cast in delta form:

$$[M - B^{-}_{j+1/2}\Delta_{j+1/2} + B^{+}_{j-1/2}\Delta_{j-1/2}]^n[M^{-1}]^n$$
$$[M - (C^{-} + C_v)_{k+1/2}\Delta_{k+1/2}$$
$$+ (C^{+} + C_v)_{k-1/2}\Delta_{k-1/2}]^n\Delta Q^n$$
$$= -RES(Q^n, Q^{n+1}) \quad (4)$$

with

$$M = I/(\Delta t J) + A^{-}_{i+1/2} + A^{+}_{i-1/2}$$

and $A = \delta E/\delta Q$, $B = \delta F/\delta Q$, and $C = \delta G/\delta Q$. The notation ΔQ^n stands for $Q^{n+1} - Q^n$ and, for instance, $\Delta_{j-1/2}() = ()_j - ()_{j-1}$. The matrices A, B, and C are split according to the sign of their eigenvalues into $A = A^{+} + A^{-}$, etc. The residual $RES(Q^n, Q^{n+1})$ contains finite-difference approximations to the spatial derivatives in Eq. (1). TVD techniques in combination with Roe's[22] flux-difference splitting give nominally up to third-order accurate discretizations of the inviscid fluxes. Conventional second-order central differencing is applied to the viscous shear fluxes. The discrete equations are solved with a first-order accurate Euler-implicit time marching procedure that employs approximate factorization (AF) in crossplanes in conjunction with a symmetric planar Gauss-Seidel (SPGS) relaxation in the remaining spatial direction.

Body Geometries and Grids

The flowfield results are computed on C-O-type grids (Fig. 2), which are generated by rotating a two-dimensional C-type grid encompassing the contours of the ogive cylinder around its longitudinal axis. The C-type grids are computed in some meridional plane as a solution to an elliptic system.[23] The outer contour of the integration domain (Fig. 2) is defined as a hemispherically capped cylinder with a radius of 28 caliber ($= 28D$). This radial extent of the integration domain ensures that the solutions are independent from the far-field boundary conditions.[16] The body geometry is defined by a 3.5-caliber tangent-ogive mounted on a 7.0-caliber cylinder.

The calculations are performed for two different tangent-ogive cylinders with slightly different surface definitions: one is axisymmetric, and the other is perturbed into elliptic cross sections just at the nose tip. Related theoretical and experimental work[9-12] suggests that asymmetric vortex flow patterns along the entire body are controlled by small surface imperfections close to the apex (i.e., $x/D = 0.0$). To model such a perturbation, the nose tip (highlighted in yellow) of the tangent ogive in Fig. 3 was slightly squashed for $x/D < 0.125$. As illustrated in Fig. 4, the ellipticity in this nose region varies linearly from a maximum value of 2.0 at $x/D = 0.0$ to a value of 1.0 at $x/D = 0.125$. The highly resolved surface definition shown in Fig. 4 has been achieved by clustering 10 cross sections in the apex regime.

Most of the calculations are carried out for both bodies on standard grids with $40 \times 145 \times 65$ grid points in longitudinal, circumferential, and radial direction, respectively. The grid points are equiangularly spaced in the circumferential direction. The stretching in radial direction is somewhat stronger than in previous work.[16] Thus, the attached boundary layers are now resolved by about 15 grid points in the radial direction, and the value for the law-of-the-wall coordinate y^+ at the first grid point off the surface varies between 0.8 along the windward part of the body surface and about 4.0 along the leeside section of the body surface. These values for y^+ lie well within the range that in earlier computational studies on F-18 forebody flows[24] was found to provide adequate viscous resolution. Although previous grid-refinement studies[16] indicated that the standard grids suffice to resolve flows with $Re_D = 0.8 \times 10^6$, some gridding effects were reassessed for the specific reason to ensure that the computed vortex asymmetries are not grid-dependent numerical artifacts. The pertinent results will be discussed below.

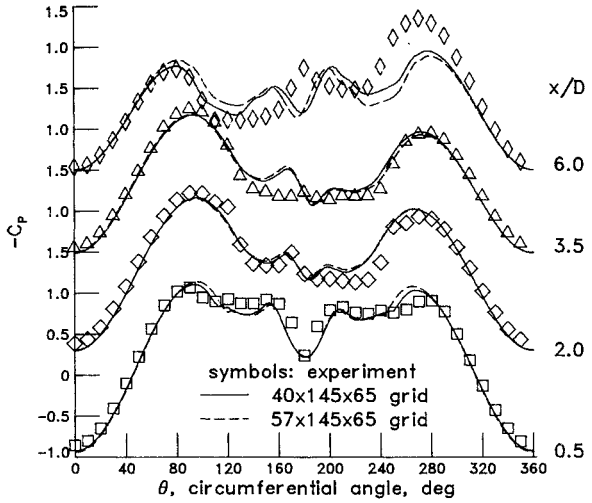

Fig. 5 Effects of longitudinal grid refinement—axisymmetric body: $\alpha = 40$ deg, $Re_D = 0.8 \times 10^6$, standard grid.

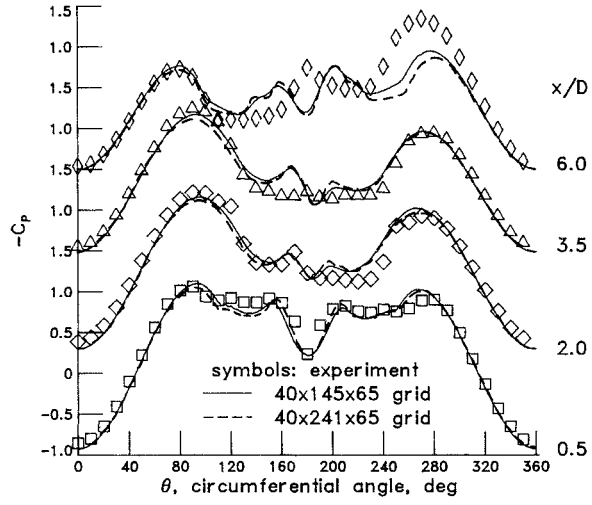

Fig. 6 Effects of circumferential grid refinement—axisymmetric body: $\alpha = 40$ deg, $Re_D = 0.8 \times 10^6$, standard grid.

Initial and Boundary Conditions

Initially, all four flow variables are set to freestream conditions except for $u = v = w = 0$ along the body surface. All boundaries are treated explicitly in time. Undisturbed freestream conditions are maintained along the far-field boundaries. The plane $x/D = 10.5 = \text{const}$ defines the outflow boundary where all velocity components are extrapolated using second-order, one-sided differences; the pressure is kept at its freestream value. In a C-O-type grid, one has a radial branch cut at some circumferential location, where the physical domain is broken up to unfold it into a regular computational domain described by a rectangular parallelepiped. To study the effects of the location of the branch cut, it was assumed to coincide with either the windward or the leeside wind plane. The boundary conditions along the branch cut were alternatively specified to be periodic boundary conditions or they were computed as averages of first- or second-order extrapolates from the interior of the integration domain. There were no discernible differences in the results due to the orientation of the branch cut or the approximation of the boundary conditions along it. A no-slip condition is applied to the body surface in combination with a limiting form of the Navier-Stokes equations along solid surfaces to compute the wall pressure.[16] The TVD-like formulation contains limiters $\phi_l^{\pm}$ ($l = i, j,$ or k)[13-16] that are set to zero along all boundaries; so are the changes ΔQ^n.

Results

The FMC1 code has been used to compute flows with $Re_D = 0.8 \times 10^6$ over a 3.5-caliber tangent-ogive cylinder at angles of attack of 20, 30, and 40 deg without imposing bilateral symmetry. Based on experimental surface pressures, transition from fully laminar to fully turbulent flow was assumed at $x/D = 1.5$. For $x/D \geq 1.5$, fully turbulent crossflow was modeled by using the Hartwich-Hall[16] extension of the algebraic turbulence model by Baldwin and Lomax.[21] For $\alpha = 20$ deg, only symmetric vortical flows have been obtained for the axisymmetric body as well as for the tangent-ogive cylinder with the squashed nose tip. In the latter case, the major axis of the elliptically deformed nose-tip cross sections were set at roll angles of 0, 45, and 90 deg. For both $\alpha = 30$ and 40 deg, all vortical flowfield results show marked vortex asymmetries. The effects of surface imperfections, of gridding, of turbulence modeling, of approximations of boundary conditions, and even of the machine accuracy have been systematically studied. Selected results will be discussed herein, which help to illustrate the physics of asymmetric vortex flow at a 40-deg angle of attack.

The results in Figs. 5 and 6 demonstrate that the vortex asymmetries are not grid-dependent artifacts. Both figures have the same layout. They compare calculated surface pressure data with Lamont's data for two axial stations on the tangent ogive ($x/D = 0.5$ and 2.0), for the junction between tangent-ogive and cylindrical afterbody ($x/D = 3.5$), and for the last station for which experimental pressure data are available ($x/D = 6.0$). The circumferential angle θ, in a pilot's view, is defined as zero at the windward wind plane and increases in clockwise direction. The standard grid results are compared with results on grids with twice the resolution in the axial direction along the tangent-ogive, not along the cylinder (Fig. 5), and almost twice the resolution in the circumferential direction (Fig. 6). All of these results were computed for the axisymmetric tip. The experimental data are given for the reference roll angle of the wind-tunnel model (i.e., the roll angle is 0 deg). Although the measured surface pressure distribution varies with roll angle, the comparisons of the calculations with the experiment in Figs. 5 and 6 are representative insofar as they show that the magnitudes of the computed surfaces pressure are close to the data at $x/D = 0.5$ and 2.0, but not quite as close at $x/D = 3.5$ and 6.0 due to a probable difference between predicted and measured shedding frequency.

Contrary to the impression one might get by looking at the results in Figs. 5 and 6, the computed vortex asymmetries are free of a bias towards the port side. Figure 7 shows a comparison of two sets of computed surface pressures for the axisymmetric body. The difference between these two computations is that one was carried out in 32-bit word arithmetic on the CYBER 205 at NASA Langley Research Center, and the other in 64-bit word arithmetic on the NAS Cray-2. These two results constitute an almost perfect mirror image to each other. Each of these results has been computed repeatedly—the answer was always the same. Thus, the present computations are, like experiments and related numerical results by Siclari and Marconi,[6] recurrent for a given computer.

The results in Figs. 8 and 9 demonstrate that the small nose tip with the elliptically deformed cross sections acts like a catalyst in forcing the asymmetric vortex pattern to assume either of Hunt's[5] two regular states for this high angle of attack. In the computation in Fig. 8, the major axis of the "elliptic" nose tip is rotated by 45 deg counterclockwise (pilot's view) out of its horizontal position. These results are compared with experimental pressure data for zero roll angle. At $x/D = 0.5$, the elliptic nose tip has a stronger effect on the circumferential pressure distribution than the presumed geometric imperfections at the nose tip of Lamont's wind-tunnel model. For the remaining three axial stations, the computed pressures match the experimental data remarkably well. In Fig. 9, the elliptic nose tip is rotated for another 90 deg, and the calculated surface pressures are compared with measured pressures for a roll angle of 90 deg. Both computations as well as experiment show the opposite regular state.

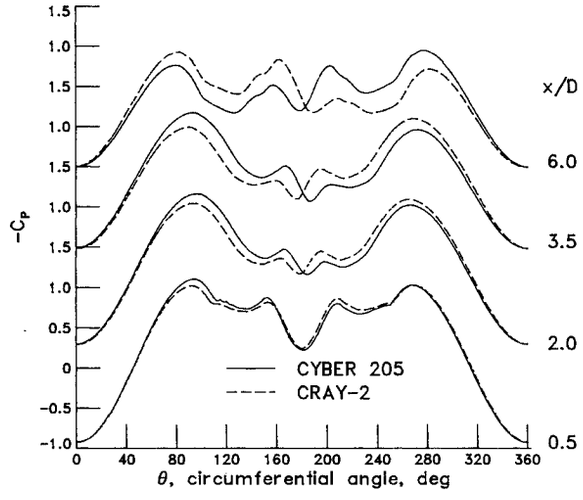

Fig. 7 Effects of machine accuracy—axisymmetric body: $\alpha = 40$ deg, $Re_D = 0.8 \times 10^6$, standard grid.

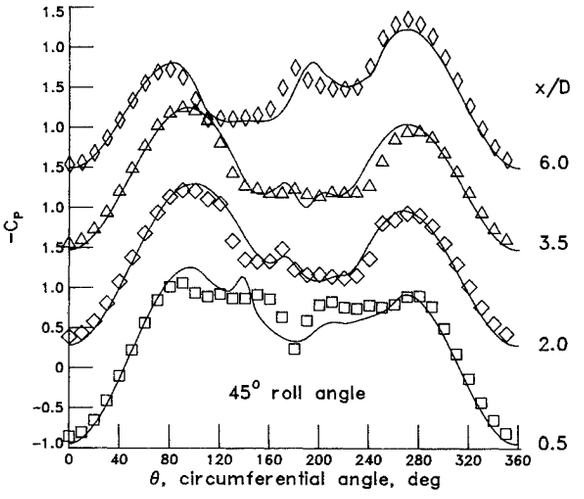

Fig. 8 Effects of elliptic nose tip: $\alpha = 40$ deg, $Re_D = 0.8 \times 10^6$, standard grid.

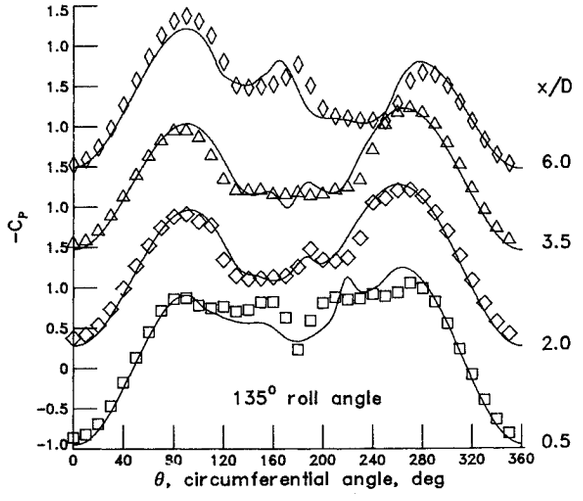

Fig. 9 Effects of elliptic nose tip: $\alpha = 40$ deg, $Re_D = 0.8 \times 10^6$, standard grid.

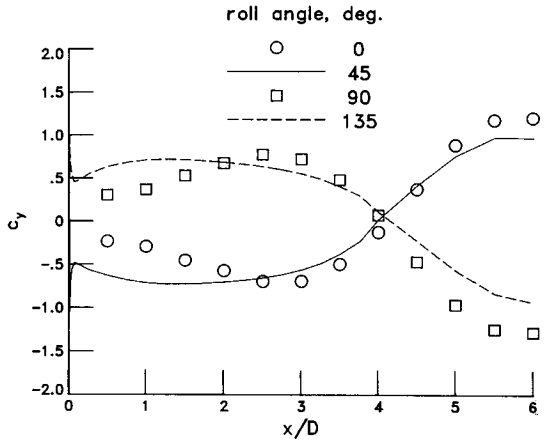

Fig. 10 Computed (lines) and measured (symbols) sectional side forces: $\alpha = 40$ deg, $Re_D = 0.8 \times 10^6$.

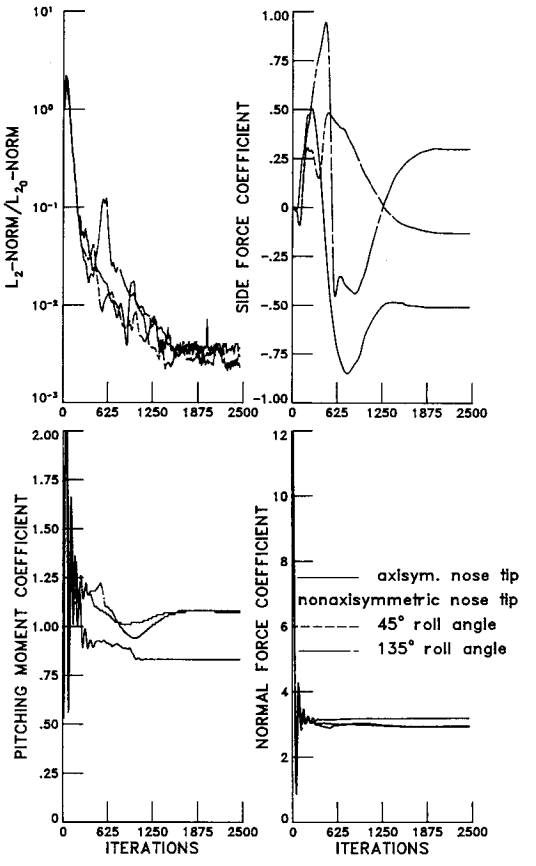

Fig. 11 Convergence summary for three computations: $\alpha = 40$ deg, $Re_D = 0.8 \times 10^6$, standard grid.

For the two cases discussed in Figs. 8 and 9, computed and measured sectional side-force coefficients (normalized with local diameter, cf. Ref. 11) are compared in Fig. 10 for $0.0 \le x/D \le 6.0$. Despite the discrepancies in the neighborhood of the apex, this comparison looks quite encouraging.

The convergence summary in Fig. 11 discloses that the asymmetric vortical flowfield results are indeed steady-state solutions to the Navier-Stokes equations. Shown are the convergence histories of normal force, pitching moment, side force, and the L_2-norms of all residuals for three sets of computations. All computations were carried out on the standard grids for $\alpha = 40$ deg and $Re_D = 0.8 \times 10^6$. The solid line reflects the convergence performance of a calculation for the fully axisymmetric body, and the two dashed lines give results for two computations with the perturbed nose tip at roll angles

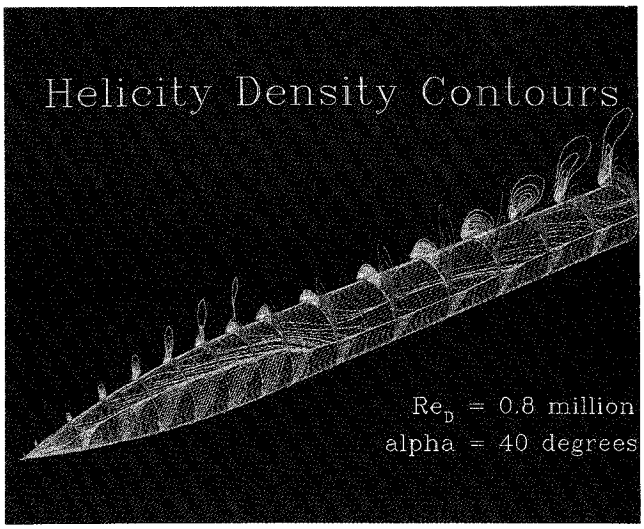

Fig. 12 Asymmetric vortex pattern.

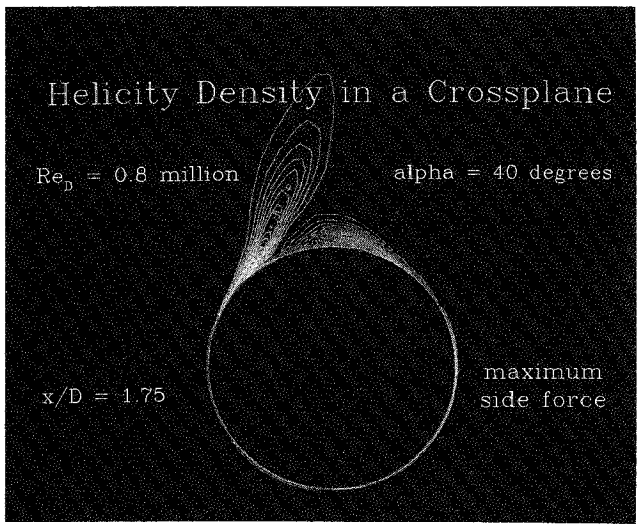

Fig. 13 Connection between crossflow pattern and maximum magnitude of local side force.

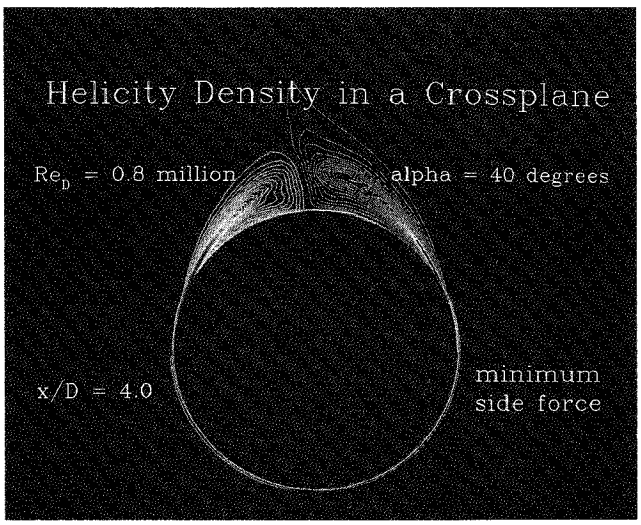

Fig. 14 Connection between crossflow pattern and minimum magnitude of local side force.

of 45 and 135 deg. Each of the calculations in Fig. 11 took about 10 h CPU time on the CYBER 205 at NASA Langley or on the NAS Cray Y-MP, and about 16 h on the NAS Cray-2. The code was run on the Crays in single-processor mode.

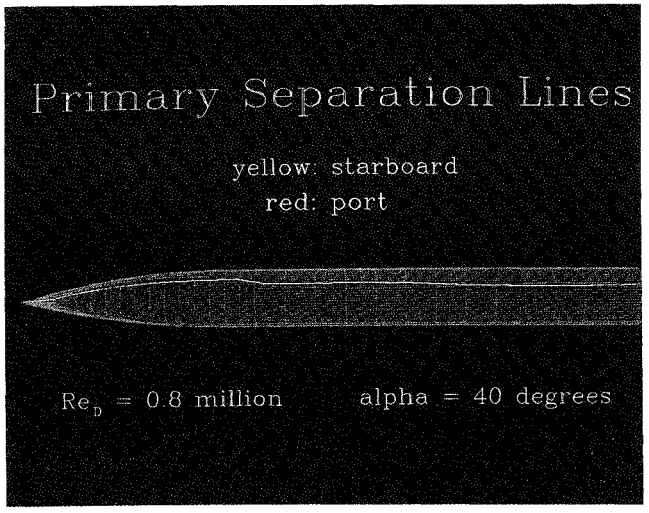

Fig. 15 Effect of vortex asymmetry on primary separation lines.

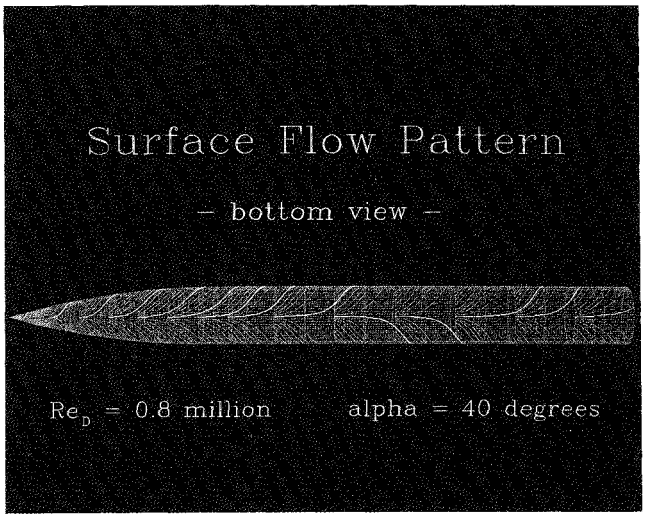

Fig. 16 Effect of vortex asymmetry on windward stagnation region.

The flowfield results used in Fig. 8 have been analyzed using computational flow-visualization techniques. Figure 12 gives an overall impression of the vortex shedding along the body. It shows cross-sectional helicity-density contours superimposed on a surface flow pattern. Helicity density is defined as the scalar product of the local velocity and vorticity vectors. Since it indicates both sense and magnitude of vorticity, it yields a viable tool to analyze the kinematics of complex three-dimensional flow by means of a scalar quantity. The "cold" colors indicate clockwise vorticity (with blue representing the maximum and green the minimum magnitude); the "hot" colors illustrate counterclockwise vorticity (with white indicating the maximum and red the minimum vorticity). The senses of rotation are defined for looking down the body in positive x direction. Starting at the apex, first a "green" primary vortex is discovered which lifts off the surface right from the start. A "red" primary vortex dominates the flow along the leeside body surface up to about $x/D = 4.0$. There, a newly formed green primary vortex has developed a strength comparable to its red counterpart. While the green vortex is still gaining strength, the red counterpart is in a state of decay as its vorticity spreads over an ever-increasing area. Finally, the red vortex sheds off the surface, and the green vortex dominates now the leeside flow along the cylinder up to about $x/D = 8.5$. There, a newly formed and rapidly growing red primary vortex is surpassing the strength of the decaying green vortex, and it is on the verge of pushing it off into the wake.

Hunt[5] raised the question about the relation between crossflow patterns and corresponding local side forces. Figures 13 and 14 show local helicity-density contours in crossplanes at $x/D = 1.75$ and 4.0. Maximum sectional side force is primarily associated with asymmetric separation in the equatorial regions; the dissimilarity of the two primary vortices has significantly less impact on the local side force since their suction is small compared to the pressure minima in the equatorial regimes (cf. Figs. 8 and 9), and because their pressure signature contributes primarily to the local normal force. In the case of minimum magnitude of local side force (Fig. 14), the primary vortices are of about equal strength and they concur with an almost symmetric arrangement of the lateral separations.

This interpretation is supported by the two primary separation lines in Fig. 15. Maximum distance between the two primary separation lines corresponds to the occurrence of maximum local side force. The crossovers of the separation lines coincide with the locations of minimum sectional side force.

There is a strong interaction between separated and attached flow as reflected by the meandering of the windward stagnation line in the bottom view in Fig. 16. The yellow streaklines are created by particles released in the windward wind plane at points adjacent to the body surface. The yellow streaklines veer off to starboard or port side corresponding to the shedding events in the wake of the body; they are pointing in the direction of the local side force.

Conclusions

Low-speed, turbulent vortex flows over two 3.5-caliber tangent-ogive cylinders have been computed as steady-state solutions to the three-dimensional, incompressible Navier-Stokes equations. The angle of attack has been varied between 20 and 40 deg; the Reynolds number has been kept at $Re_D = 0.8 \times 10^6$. One configuration is axisymmetric and the other has a nose tip whose cross-sectional shape is slightly elliptic. A recurrent bifurcation of the asymmetric solution for subsonic flow over an axisymmetric slender body was triggered by machine accuracy. The calculations for the body with the perturbed nose-tip geometry agreed well with experimental data. This supports earlier conjectures that slight imperfections in the neighborhood of the apex of slender bodies with sharp noses determine the asymmetric flow pattern along the entire body. Computational flow visualization disclosed the connection between minimum and maximum magnitude of local side force values and the local cross-sectional state of the flow.

Acknowledgments

NASA Langley Research Center supported the work of the first and third authors under Contracts NAS1-18585 and NAS1-18000, respectively.

References

[1]Skow, A. M., and Erickson, G. E., "Modern Fighter Aircraft Design for High Angle-of-Attack Maneuvering," AGARD-LS-121, Paper No. 4, 1982.

[2]Keener, E. R., Chapman, G. T., Cohen, L., and Talaghani, J., "Side Forces on Forebodies at High Angles of Attack and Mach Numbers of 0.1 to 0.7: Two Tangent Ogives, Paraboloid, and Cone," NASA TM-X-3438, Feb. 1977.

[3]Lamont, P. J., "The Effect of Reynolds Number on Normal and Side Forces on Ogive Cylinders at High Incidence," AIAA Paper 85-1799, Aug. 1985.

[4]Ericsson, L. E., and Reding, J. P., "Asymmetric Vortex Shedding from Bodies of Revolution," *Progress in Astronautics and Aeronautics: Tactical Missile Aerodynamics,* Vol. 104, edited by M. J. Hemsch and J. N. Nielsen, Washington, DC, 1986, pp. 243–382.

[5]Hunt, B. L., "Asymmetric Vortex Forces and Wakes on Slender Bodies," AIAA Paper 82-1336, Aug. 1982.

[6]Siclari, M. J., and Marconi, F., "The Computation of Navier-

Stokes Solutions Exhibiting Asymmetric Vortices," AIAA Paper 89-1817, June 1989.

[7]Fiddes, S. P., "Separated Flows About Cones at Incidence—Theory and Experiment," *Studies of Vortex-Dominated Flows,* Springer-Verlag, New York, 1987, pp. 185–310.

[8]Marconi, F., "Asymmetric Separated Flows About Sharp Cones in a Supersonic Stream," *Lecture Notes in Physics,* Vol. 323, Springer-Verlag, New York, 1989, pp. 395–402.

[9]Moskovitz, C. A., Hall, R. M., and DeJarnette, F. R., "Effects of Surface Perturbations on the Asymmetric Vortex Flow Over a Slender Body," AIAA Paper 88-0483, Jan. 1988.

[10]Moskovitz, C. A., Hall, R. M., and DeJarnette, F. R., "Effects of Nose Bluntness, Roughness, and Surface Perturbations on the Asymmetric Flow Past Slender Bodies at Large Angles of Attack," AIAA Paper 89-2236, July 1989.

[11]Hall, R. M., "Forebody and Missile Side Forces and the Time Analogy," AIAA Paper 87-0327, Jan. 1987.

[12]Hall, R. M., "Influence of Reynolds Number on Forebody Side Forces for 3.5-Diameter Tangent-Ogive Bodies," AIAA Paper 87-2274, Aug. 1987.

[13]Hsu, C.-H., Hartwich, P.-M., and Liu, C. H., "Computation of Vortical Interaction for a Sharp-Edged Double-Delta Wing," *Journal of Aircraft,* Vol. 25, No. 5, 1988, pp. 442–445.

[14]Hartwich, P.-M., Hsu, C.-H., and Liu, C. H., "Vectorizable Implicit Algorithms for the Flux-Difference Split, Three-Dimensional Navier-Stokes Equations," *ASME Journal of Fluids Engineering,* Vol. 110, No. 3, Sept. 1988, pp. 297–305.

[15]Hartwich, P.-M., and Hsu, C.-H., "High-Resolution Upwind Schemes for the Three-Dimensional, Incompressible Navier-Stokes Equations," *AIAA Journal,* Vol. 26, No. 11, 1988, pp. 1321–1328.

[16]Hartwich, P.-M., and Hall, R. M., "Navier-Stokes Solutions for Vortical Flows Over a Tangent-Ogive Cylinder," *AIAA Journal*, Vol. 28, No. 7, 1990, pp. 1171–1179; see also Erratum in Vol. 28, No. 10, 1990, pp. 1848–1849.

[17]Peyret, R., and Viviand, H., "Computations of Viscous Compressible Flows Based on the Navier-Stokes Equations," AGARD-AG-212, Sept. 1975.

[18]Chorin, A. J., "A Numerical Method for Solving Incompressible Viscous Flow Problems," *Journal of Computational Physics,* Vol. 2, No. 1, Aug. 1967, pp. 12–26.

[19]Steger, J. L., and Kutler, P., "Implicit Finite-Difference Procedures for the Computation of Vortex Wakes," *AIAA Journal,* Vol. 15, No. 4, pp. 581–590.

[20]Rizzi, A., and Eriksson, L. E., "Computation of Inviscid Incompressible Flow with Rotation," *Journal of Fluid Mechanics,* Vol. 49, March 1985, pp. 327–393.

[21]Baldwin, B. S., and Lomax, H., "Thin-Layer Approximation and Algebraic Turbulence Model for Separated Turbulent Flows," AIAA Paper 78-257, Jan. 1978.

[22]Roe, P. L., "Approximate Riemann Solvers, Parameter Vectors, and Difference Schemes," *Journal of Computational Physics,* Vol. 43, No. 2, Oct. 1981, pp. 357–372.

[23]Hartwich, P.-M., "Three-Dimensional Grids as Solutions of Elliptic Systems," AIAA Paper 86-0430, Jan. 1986.

[24]Ghaffari, F., Luckring, J. M., Thomas, J. L., and Bates, B. L., "Navier-Stokes Solutions about the F/A-18 Forebody-LEX Configuration," AIAA Paper 89-0338, Jan. 1989.

Walter B. Sturek
Associate Editor

Color reproduction courtesy of ViGYAN, Inc.